Accepted in *Journal of Crystal Growth* 579 (2022) 126461

A Temperature-Dependent Atomistic-Informed Phase-Field Model to Study Dendritic Growth

Sepideh Kavousi, Austin Gates, Lindsey Jin, and Mohsen Asle Zaeem*

Department of Mechanical Engineering, Colorado School of Mines, Golden, CO 80401, USA

Abstract

The effects of solid-liquid interface anisotropy and kinetics on crystallization of highly undercooled titanium melts are studied by coupling molecular dynamics and phase-field simulations. Unlike previous models and to consider the actual physics of crystal growth, the phase-field parameters, representing interface mobility, solid-liquid transformation barrier, and interfacial energy gradient, are temperature dependent. The parameters are determined by a combination of molecular dynamics simulations and classical thermodynamic calculations based on the temperature-dependent solid-liquid interface properties and kinetic coefficient. We investigated Ti dendritic growth as a benchmark example to demonstrate that the phase-field model presented in this work is more compatible with the experimental data and theoretical models in comparison to the earlier models with constant model parameters. The capillary fluctuation method is used to determine the solid-liquid interface energy and its anisotropy for undercoolings up to 400 K. Similar to theoretical models, the average solid-liquid interface energy decreases with temperature, and the preferred dendrite growth direction shifts from <100> to <110> direction as the undercooling increases. Phase-field simulations also show other favorite growth directions, implying that there is a competition between the interface anisotropy and kinetics of the solid-liquid interface.

Keywords: A1. Computer simulation, A1. Dendrites, A1. Solidification.

*Corresponding author: zaeem@mines.edu (M. Asle Zaeem)

1. Introduction

In solidification, formation and evolution of solid-liquid (SL) interface affect the microstructures and properties of solidified metals and alloys [1]. The solid-liquid interfacial energy and its anisotropy and solidification kinetics are some of the key factors affecting different stages of solidification, such as nucleation, pattern selection, and final morphology [2]. Phase-field (PF) modeling of solidification for a few single element metals and binary alloys has highlighted the sensitivity of PF results to anisotropic SL interfacial properties [3-5]. Most of the PF models in literature [6-8] are developed to simulate slow solidification with small undercooling, and employing them for investigating rapid solidification results in some deviations from the experimental predictions [9, 10].

Inaccuracy of the PF model to predict velocity-undercooling behavior for solidification of highly undercooled Ni melt was attributed to the formulation of PF model by Bragard et al. [9]. They showed that one-dimensional (1D) steady-state solution of PF equations presents a concave behavior as undercooling exceeds a limit. Therefore, they modified the energy term such that, for a large undercooling, the velocity-undercooling relationship fits to the same linear behavior as for small undercooling. Kavousi et al. [10] used the same method to modify the PF model so the results for solidification of pure Ti get closer to experiments [11, 12]. Despite the brilliance of this technique, it does not modify the PF model based on a physical phenomenon; also, this method requires obtaining 1D steady-state solution of the PF model for the material of interest to quantify the power-law driving force function in the PF model. Besides, experimental studies suggest that the Gibbs free energy maintains a linear relationship with undercooling unless it exceeds 0.2 times the melting point, which was not the case for the aforementioned experiments [11-14] and PF studies [11, 12].

The second problem with PF simulations of highly-undercooled metals is the fact that PF parameters are determined based on interfacial properties at the melting point, while some previous studies showed that the SL interface energy changes with temperature [15, 16]. Determining the SL interfacial energy using experimental methods is an intensive and difficult process. Grain boundary groove, developed by Gunduz and Hunt [17], is the most common technique used to find the interfacial energy in alloys. In this method, the SL interface is equilibrated with a grain boundary under a temperature gradient, such that it establishes a planar SL interface except close to the grain boundary. Thus, the interface energy is obtained by measuring the equilibrium shape of the groove's profile [3]. This method has been used to estimate the SL interface energy for different binary [18, 19], and eutectic [20, 21] systems. This method cannot be used to obtain the interface energy for pure metals, and they are mostly obtained by extrapolating the relationship between concentration and SL interface energy [22]. Homogeneous nucleation in undercooled conditions is another method used by Turnbull in the 1950s to determine SL interfacial energy [23]. This method is based on the nucleation theory where the interface energy is estimated by calculating nucleation frequencies of small droplets. The existence of inevitable heterogeneous nucleation sites leads to deviation in results associated with this method in comparison to other experimental techniques and theoretical predictions [22, 24]. Although the homogenous nucleation method can calculate the interface energy at the critical undercooled temperature, to the best of our knowledge, there is no experimental study that reports the temperature-dependent SL interface energy.

The challenges in direct calculations of interfacial properties, especially for the temperature-dependent values, have made atomistic modeling a popular choice for calculating the target material properties [2] and investigating the mechanisms governing different stages of nucleation process [25-27] . Capillary fluctuation method (CFM) is a computational technique to calculate the interface energy [28, 29]. In this method, interface free energy is estimated based on the spectrum of interfacial fluctuations. Repeating the simulations for multiple orientations along the interface normal enables obtaining the stiffness for various orientations which are used to obtain the mean SL interfacial energy and the corresponding anisotropy terms [28, 29]. CFM has been used to study the temperature-dependent interface energy for Cu-Zr [16] and Cu-Ni [30] binary systems. Critical nucleation theory (CNT) is another method to obtain the interface energy of undercooled melt [31, 32]. But this method does not provide any information about the anisotropy values. In the quest for determining temperature-dependent interface energy, Wu et al. combined the CFM and CNT to obtain the anisotropic interface energy of Al at a wide range of temperatures [33]. Laird et al. estimated the SL interface energy in an undercooled Lennard-Jones melt based on the Gibbs-Cahn integration method [34].

In this study, we develop a new PF model considering temperature-dependent model parameters. The dependence of material properties on temperature is obtained by molecular dynamics (MD) simulations. First, details of PF model are provided and the PF parameters are determined as a function of temperature. The temperature-pressure coexistence curve is calculated followed by CFM calculations of the interfacial energy. Then, MD calculations of Gibbs-Helmholtz equation are performed to test the validity of nonlinear relationship between the Gibbs free energy and temperature proposed by Bragard et al. [9] . Finally, PF simulations of solidification are performed. The PF model is validated by comparing velocity-undercooling relationship to the experimental data. The competing effect of undercooling and anisotropy on dendritic morphology is investigated.

2. Phase-Field Model

Instead of direct tracking of the SL interface, phase-field model introduces a variable called order parameter (ϕ) to describe the interface between the two phases [35]. Order parameter takes constant values in solid and liquid, 1 and 0, respectively, and changes with a sharp but continuous function along the interface. The time evolution equations of ϕ and temperature (T) are used to describe the solidification of metals. The governing equation for the order parameter is obtained by taking the functional derivative of the Ginzburg-Landau type free energy, F, given by Equation (1).

$$F = \int \left[f_{dw}(\phi, T) + \frac{\varepsilon(T,\hat{n})^2}{2} |\nabla\phi|^2 \right] dV \ , \tag{1}$$

$$f_{dw}(\phi, T) = w(T)g(\phi) + q(T, \phi) \ . \tag{2}$$

First term on the right-hand-side of Equation (1) is the bulk free energy (f_{dw}), and the second term describes the excess free energy due to the interface, where ε is a parameter related to the magnitude of the interface energy. As given by Equation (2), f_{dw} consists of two terms; the first term is the double-well Ginzburg-Landau free energy function, $w(T)g(\phi)$, where $g(\phi) = \phi^2(1-\phi)^2$ is the double well function and $w(T)$ is the temperature-dependent height of the well. All the PF models in literature consider the well-size to be constant [6, 7, 36], but the process of atom addition to a cluster is diffusion controlled. For a thermally activated jump between the neighboring sites, jump frequency (υ) can be described as [37]:

$$\upsilon \propto e^{-\frac{Q}{\mathrm{k_B}T}} \ , \tag{3}$$

where Q is the activation energy, and $\mathrm{k_B}$ is the Boltzmann constant. Therefore, for a constant activation energy, jump frequency will reduce by a decrease in temperature. While in PF formulation, the effect of temperature on the jump frequency is neglected, and the well's height is estimated based on material properties at the melting point. To address the temperature dependence of jump frequency in the PF model, we consider that the well's height used in PF equations undergoes a correction, as shown in Equation (4). This equation results in an increase of the well's height with temperature such that it dictates the desired change in jump frequency.

$$w(T) = \mathrm{w}_0 \frac{T}{\mathrm{T_m}} . \tag{4}$$

The second term in Equation (2), $q(T, \phi)$, represents the temperature-dependent free energies of both solid and liquid phases. In the classical thermodynamics, two assumptions are made for the SL phase transformations for a small undercooling. First, difference between the entropies of solid and liquid phases in an undercooled system can be assumed to take an equal value at the melting point ($\mathrm{T_m}$). Besides, the enthalpy of fusion ($\mathrm{L_0}$) is assumed to be independent of temperature [1]. Based on our MD simulation results, which will be presented in Figure 5, assuming a linear relationship between the solid or liquid enthalpies with temperature is valid for undercooling as large as 0.2 times the melting point [23]. Therefore, the resulted difference between free energy densities of the solid and liquid phases in the previous PF models is:

$$f_{dw}(\phi = 1) - f_{dw}(\phi = 0) = \frac{\mathrm{L_0}}{\mathrm{T_m}}(T - \mathrm{T_m}). \tag{5}$$

Taking the free energy of the liquid phase as reference state and considering $h(\phi) = \phi^3(10 - 15\phi + 6\phi^2)$ as the smoothing function for temperature-dependent energy term, the final form of bulk free energy becomes:

$$f_{dw}(\phi, T) = w(T)g(\phi) + h(\phi)\frac{\mathrm{L_0}}{\mathrm{T_m}}(T - \mathrm{T_m}) . \tag{6}$$

Second term in the right-hand-side of Equation (1) describes the excess free energy due to interface. The dependence of ε on orientation and temperature is described based on the anisotropic temperature-dependent SL interface energy following the thin interface analysis. Thin interface analysis maps PF equations to the classical sharp-interface equations for solidification [38]. This allows linking the phase field parameters ε , w, and M, which are directly related to the interface energy, well-height, and interface mobility, respectively, to the material properties that are calculated from MD simulations such as SL interfacial free energy and kinetic coefficient [6].

$$\zeta_p(\mathrm{T}) = \frac{\varepsilon_0(T)}{\sqrt{w(T)}} 2\sqrt{2}\, ln3 \, , \tag{7}$$

$$\gamma(T,\hat{n}) = \frac{\varepsilon(T,\hat{n})\sqrt{w(T)}}{3\sqrt{2}} \, , \tag{8}$$

$$\frac{1}{\mu(\hat{n})} = \frac{1}{3\sqrt{2}} \frac{\mathrm{T_m}\sqrt{w(T)}}{\varepsilon(T,\hat{n})\mathrm{L_0}M(T,\hat{n})} - \frac{\mathrm{L_0}}{\mathrm{Dc_p}} \frac{\varepsilon(T,\hat{n})}{\sqrt{2w(T)}} \int_0^1 \frac{h(\phi)(1-h(\phi))}{\sqrt{g(\phi)}}\, d\phi \, . \tag{9}$$

D is the thermal diffusivity, $\mathrm{c_p}$ is the specific heat, and ζ_p is the interface thickness which is set to be larger than the microscopic capillary length (d_0) described by

$$d_0 = \frac{\gamma_0}{\mathrm{L_0}} \, . \tag{10}$$

γ_0 is the orientation-averaged SL interface energy. For a crystal with cubic symmetry, the SL interfacial free energy (γ) as a function of orientation and temperature can be represented by the following equation [39]:

$$\gamma(T,\hat{n}) = \gamma_0(\mathrm{T})\ [1 + \delta_1(T)\left(\sum_{i=1}^{3} n_i^4 - \frac{3}{5}\right) + \delta_2(\mathrm{T})\ (3\ \sum_{i=1}^{3} n_i^4 + 66 n_1^2 n_2^2 n_3^2 - 17/7)] \, , \tag{11}$$

where n_i are the components of the unit vector normal to the interface plane ($\hat{n}$), and δ_1 and δ_2 are the anisotropy parameters. In this study, we will consider γ_0, δ_1 and δ_2 to be a function of temperature and use MD simulations to quantify them. Similarly, the kinetic coefficient follows a similar equation given by [40]:

$$\frac{1}{\mu(\hat{n})} = \frac{1}{\mu_0}(1 + 3\varepsilon_k - 4\varepsilon_k \sum_{i=1}^{3} n_i^4) \, . \tag{12}$$

μ_0 is the average kinetic coefficient, and ε_k is the corresponding anisotropy parameter.

The final form of evolution equations for ϕ and T are given by:

$$\frac{1}{M(T,\theta)}\frac{\partial\phi}{\partial t} = \nabla.(\varepsilon(T,\theta)^2\nabla\phi) + \frac{\partial\left(\varepsilon(T,\theta)\varepsilon'(T,\theta)\frac{\partial\phi}{\partial x}\right)}{\partial y} - \frac{\partial\left(\varepsilon(T,\theta)\varepsilon'(T,\theta)\frac{\partial\phi}{\partial y}\right)}{\partial x} - w(T)g'(\phi) - h'(\phi)\frac{L_0}{T_m}(T - T_m) + Noise(\phi) \, , \tag{13}$$

$$\frac{\partial T}{\partial t} = D\nabla^2 T + \frac{L_0}{c_p} h'(\phi) \frac{\partial \phi}{\partial t} \, . \tag{14}$$

3. Results and Discussion

We perform atomistic-informed PF simulations of solidification of Ti to investigate accuracy of the developed temperature-dependent MD-PF framework for dendrite growth. This section starts with the details of MD simulations for obtaining the material properties, followed by PF simulations to investigate the solidification of highly-undercooled Ti. All MD simulations are performed using the LAMMPS software (Large-scale Atomic/Molecular Massively Parallel Simulator) [41], and MEAM interatomic potential developed by Kavousi et al. [42] is used to describe the atomic interactions. In development of this potential, the accuracy of high temperature kinetic and interfacial properties was targeted.

3.1. Molecular dynamics simulations to calculate temperature-dependent material properties

CFM is used to obtain the dependence of SL interface energy on temperature. Employing CFM requires prior knowledge of the temperature(T)-pressure(P) coexistence curve. Each point on the coexistence curve is obtained through a series of simulations. The first simulation starts from a system with 10×10×120 unit cells (24,000 atoms), where central half of the system is melted. For each desired pressure, the system is equilibrated for 1000 ps through the isothermal-isobaric (NPT) ensemble at an initial guess for temperature (T_0). It is then followed by an isenthalpic (NPH) ensemble for ~10 ns. NPH ensembles do not allow the total enthalpy change, therefore the energy must be directed through temperature change. If the difference between T_0 and the average temperature of the last 2 ns of NPH ensemble (T_1) exceeds 4K, then the simulation will restart using T_1 as the initial working temperature for Nose-Hoover thermostats. As an example presented in Figure 1(a), a system with P=-7 GPa required 4 sets of calculations such that the difference between convergence temperature drops below 4K. The error bars are obtained based on standard deviation of the temperature during the last 2 ns of the NPH ensemble. Figure 1(b) summarizes the coexistence line obtained for Ti which is obtained directly from MD calculations. The calculated errors for MD simulation datapoints in Figure 1(b) are given in Table 1. Based on Clausius–Clapeyron equation, the slope of coexistence curve for two condense phases on the temperature-pressure diagram is given by [43]:

$$\frac{dP}{dT} = \frac{L_0}{T\Delta v}\,. \tag{15}$$

Δv is the volume change during phase transformation. Later, we will show that the enthalpy of fusion has a weak dependency on temperature. Therefore, the dashed line in Figure 1(b) is obtained using the pressure-dependent enthalpy of fusion and volume change, which are estimated by a series of separate MD simulations. There is a good agreement between the direct calculations of coexistence line and predictions of Clausius–Clapeyron equation for the interface temperature higher than ~1750 K.

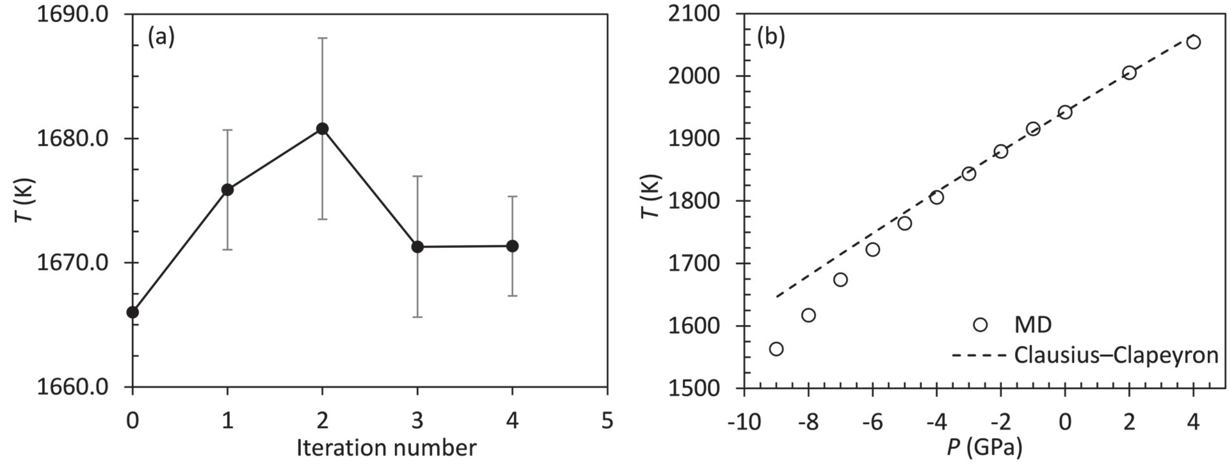

Figure 1. (a) Temperature change over the number of iteration at P=-7GPa, and (b) temperature-pressure coexistence curve calculated by MD simulations and Clausius–Clapeyron equation.

Table 1. The temperature-pressure coexistence line values for pressures between 4 and -9 GPa. The error is estimated based on the standard deviation of the temperature during the last 2 ns of the NPH ensemble.

P (GPa)	4	2	0	-1	-2	-3	-4	-5	-6	-7	-8	-9
T (K)	2054 ±7.8	2005 ±5.8	1942 ±4.56	1915 ±4.57	1879 ±6.7	1843 ±4.5	1806	1764 ±4	1722	1674 ±5.1	1617 ±4	1563

CFM estimates the SL interface energy based on its fluctuations. In this method, the interface stiffness, $\gamma + d^2\gamma/d\,\theta^2$, is related to the amplitude of interface fluctuations based on Equation (18). In this equation, bW is the interface cross-section area, k is the mode number, and $A(k)$ is the Fourier amplitude used to determine the fluctuations of instantaneous interface position

$h(x)$ from its average value $\langle h \rangle$, Equation (16). Details of MD simulations and the analysis performed to define the accurate position of interface are discussed in our previous works [10, 44].

$$h(x) - \langle h \rangle = \sum_k A(k)\, e^{ikx} \; , \tag{17}$$

$$\gamma + d^2\gamma / d\,\theta^2 = \frac{\mathrm{k_B} T}{\mathrm{bW}\langle |A(k)|^2 \rangle k^2} . \tag{18}$$

As presented by Equation (11), the interface energy is an anisotropic property and therefore MD simulations are performed for multiple SL interface orientations, presented in Table 2. {} denotes the interface normal orientation, and < > denotes one of the interface's in-plane crystallographic orientations. Using the interface stiffness calculated by each MD simulation and expressions presented in Table 2, one can calculate the mean SL interface and the corresponding anisotropy parameters.

Figure 2 summarizes the parameters entering Equation (11) obtained by the best fit to MD data for the temperature range between 1643 K and 1943 K. The calculated SL interface energy at melting point is 0.169 J/m^2, which is close to the experimental value of 0.164 J/m^2 [45]. As a validation of our temperature-dependent SL interfacial free energy calculations, Thomson-Spaepen (TS) relationship is used, given by [46]:

$$\gamma = \alpha \Delta S_m (\mathrm{N} V_m^2)^{-1/3} T_I \; , \tag{19}$$

where α=0.71 for body-centered cubic crystals, ΔS_m denotes the entropy of fusion, N is Avogadro number, V_m is the molar volume of the solid phase, and T_I is the interface temperature. Despite ~10% difference between the MD simulation results and the predictions of analytical TS relationship in Figure 2, the slope of SL interface energy change with temperature for both methods is very close.

Table 2. The expressions for the SL interface energy and stiffness for various interface orientations as given by Equation (11).

Interface orientation	Interface free energy expression	Interface stiffness expression
$\langle 100 \rangle \{001\}$	$\gamma_0 [1+0.4\, \delta_1 +0.57\, \delta_2]$	$\gamma_0 [1- 3.6\, \delta_1 - 11.43\, \delta_2]$
$\langle 1\bar{1}0 \rangle \{110\}$	$\gamma_0 [1-0.1\, \delta_1 -0.93\, \delta_2]$	$\gamma_0 [1+ 3.9\, \delta_1 + 11.07\, \delta_2]$
$\langle 001 \rangle \{110\}$	$\gamma_0 [1-0.1\, \delta_1 -0.93\, \delta_2]$	$\gamma_0 [1- 2.1\, \delta_1 + 26.07\, \delta_2]$

$\langle 1\bar{1}0\rangle\ \{111\}$	$\gamma_0\,[1-0.27\,\delta_1+1.02\,\delta_2]$	$\gamma_0\,[1+2.4\,\delta_1-20.32\,\delta_2]$
$\langle 11\bar{2}\rangle\ \{111\}$	$\gamma_0\,[1-0.27\,\delta_1+1.02\,\delta_2]$	$\gamma_0\,[1+2.4\,\delta_1-20.32\,\delta_2]$

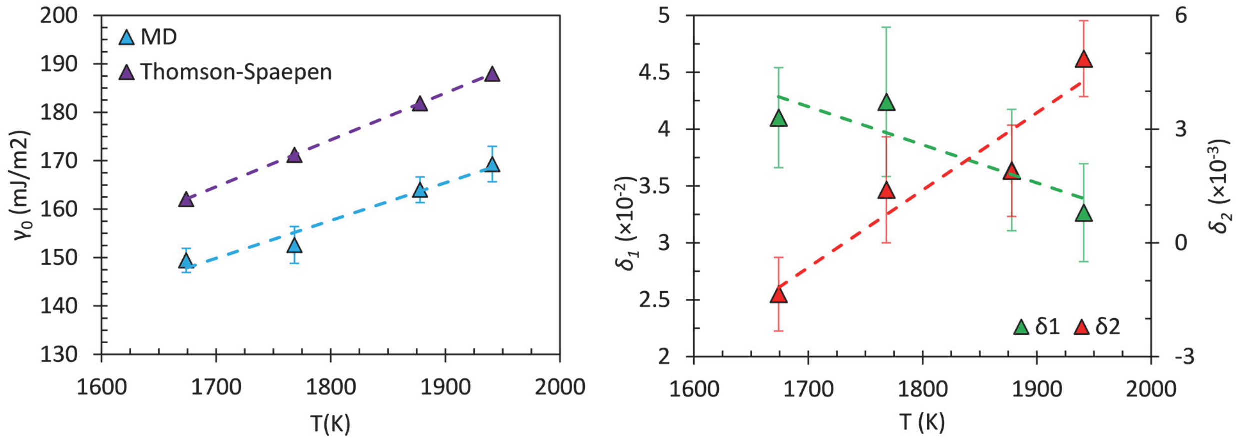

Figure 2. Temperature-dependent interface energy and anisotropy parameters. The error bars are based on 95% confidence intervals.

In obtaining the solid-liquid interface free energy for each point on the pressure-temperature coexistence line, we considered both the effects of pressure and temperature. The variations of both T and P may have significant effects on the solid-liquid interface equilibrium of the system. We used the Clausius-Clapeyron equation (Equation (15)) to determine the relationship between pressure and temperature. However, our PF simulations and the experimental works that are used for validating the PF model are non-pressurized solidification problems, and the undercooling is the sole driving force for the phase transformation. Thus, we should ensure that the effect of pressure on the calculated solid-liquid interface energy is negligible. We use the method developed by Frolov and Mishin [47], where the solid-liquid surface stress is calculated with the solid-liquid interface free energy and its variation with the interface area. The relationship between these two quantities is given by:

$$\tau = \gamma + A\frac{\partial \gamma}{\partial A} \quad , \tag{20}$$

where τ is the average surface stress given by $\tau = (\tau_{11} + \tau_{22})/2$. Based on the magnitude of derivative of interface free energy with respect to the interface area (A), τ and γ can be different in sign and magnitude. γ is always a positive number [10], while τ can be larger than γ, smaller, or even a negative number, and their difference is an important factor in the nucleation theory. In the nucleation of solid particles from a liquid, the difference between the chemical potentials of components inside the phases is proportional to $\gamma - \tau$. By applying the Cahn's adsorption equation [48] to the nonhydrostatic case of a planar solid-liquid interface, Frolov and Mishin related the total excess free energy due to the solid-liquid interface to the number of atoms (N), volume (V), and total virial stress ($\sigma_{ij} + \delta_{ij}p$) which consists of the average stress tensor and pressure [47]. The final expression that they proposed for calculating the solid-liquid surface stress is given by:

$$\tau_{ij} = \frac{[(\sigma_{ij}+\delta_{ij}p)V/NV]}{A} = \frac{det\begin{pmatrix} [(\sigma_{ij}+\delta_{ij}p)V] & [N] & [V] \\ (\sigma_{ij}+\delta_{ij}p)V^s & N^s & V^s \\ 0 & N^l & V^l \end{pmatrix}}{A \times det\begin{pmatrix} N^s & V^s \\ N^l & V^l \end{pmatrix}}. \tag{21}$$

The square brackets refer to obtaining the average properties inside a region thick enough to contain the interface, and *s* and *l* refer to the values obtained inside the bulk solid and liquid phases, respectively. Studies in the literature suggest that when γ and τ have the same order of magnitude, the effect of pressure on the solid-liquid interface energy is negligible [47, 49]. We analyzed the MD results to calculate the variations of τ with temperature. As shown in Figure 3, the surface stress decreases with the decrease in temperature. Despite the difference between the γ and τ obtained by MD, their difference is not as large as the essential threshold (one order of magnitude) for considering the dependance of γ on pressure. Thus, we can conclude that the effect of pressure on the interface energy values is negligible, and we can use the solid-liquid interface energies, given by Figure 2, in the PF modeling of solidification.

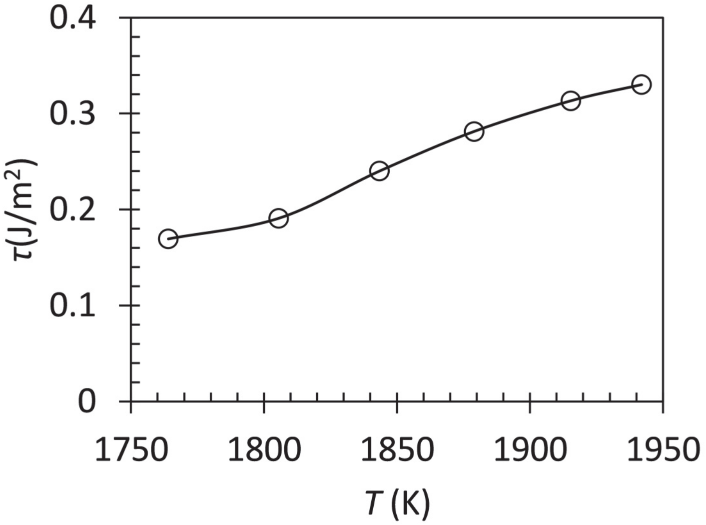

Figure 3 Temperature-dependent solid-liquid interface stress obtained by MD simulations.

Kinetic coefficient (μ) for solidification is another material property that affects the solidification microstructure. Free solidification method is a well-known technique to estimate this property using MD simulations. In this study, we use the available value reported in our previous work [10]. Equations (4), (7)-(9) are used to determine the PF parameters, based on the MD-calculated material properties.

3.2. Temperature effect in PF modeling of highly undercooled system

Before making further discussions on the results of our proposed PF model, we use MD simulations to test the validity of our model versus another PF model which was used for investigating rapid solidification of pure material developed by Bragard et al. [9]. As discussed previously, Bragard et al. [9] assumed that a linear relationship between the temperature and free energy does not hold as the undercooling increases. Therefore, they proposed changing their PF model free energy formulation from a linear to temperature dependent power-law form, where the power is obtained based on the 1D steady-state solution of order parameter evolution equation. Specifically, in a 1D system where the reference frame translating with velocity V_n along the +x direction, Equation (13) can be rewritten as:

$$-\frac{V_n}{M}\frac{\partial\phi}{\partial x} = \varepsilon^2\frac{\partial^2\phi}{\partial x^2} - wg'(\phi) - h'(\phi)\frac{L_0}{T_m}\Delta T. \qquad (22)$$

In PF modeling, the order parameter holds a constant value inside bulk phases and changes monotonically at regions close to the SL interface. Equation (23) is the equilibrium 1D solution of the order parameter equation [50].

$$\phi = \frac{1}{2}\left(1 - tanh\left(\frac{x}{\sqrt{2}\zeta_p}\right)\right). \tag{23}$$

For each undercooling, there is only one specific value of V_n, which makes the order parameter given by Equation (23) a valid solution for Equation (22) [9]. We employed *bvp4c* solver in MATLAB [51] to solve the aforementioned boundary value problem. Figure 4 presents the variation of interface velocity with the undercooling, when the PF parameters are calculated based on the fixed and temperature dependent material properties. For constant material properties, there is a perfect linear relationship between the velocity and undercooling when ΔT<150. As the undercooling exceeds 150 K, the system fails to keep the linear correlation. In order to mitigate this shortcoming, Bragard et al. [9] proposed altering the temperature-dependent term in free energy function to follow $V_n^{-1}(\Delta T)$ (inverse of the function V_n), such that the PF results are mapped onto the dashed line in Figure 4. Based on the hypothesis of Braggard et al., 150 K undercooling is the threshold for the transition of Gibbs free energy, i.e. undercooling behavior for Ti. On the other hand, the experimental study [23] on different materials, such as Ni, Co, Fe, Ag, Au, etc., suggests Gibbs free energy maintains a linear relationship with undercooling unless ΔT exceeds 0.2 times the melting point. Therefore the 150 K threshold suggested by Bragard's model (0.077 × melting point) does not meet the experimental requirements. We use MD simulations to have a deeper understanding on this matter.

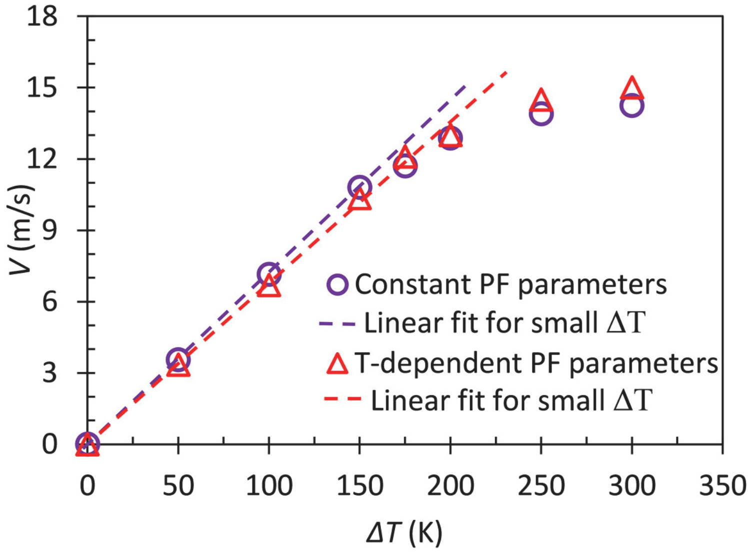

Figure 4. Variation of the steady-state velocity of a planar 1D interface with undercooling for constant and temperature-dependent PF parameters. The dashed lines are linear fits for small undercooling.

Using the Gibbs-Helmholtz relation, given by Equation (21), one can obtain the difference between free energies of the solid and liquid phases (ΔG) for metallic systems.

$$\Delta G(T) = T \int_{T}^{T_m} \frac{H^S(T\prime) - H^L(T\prime)}{T\prime^2} dT'. \tag{24}$$

T' is the integration variable, T_m is the melting temperature, H^S, and H^L are the enthalpies of solid and liquid phases, respectively. For the temperature range of 1643 to 1943 K, MD simulations are performed to determine the enthalpy of both solid and liquid phases using an NPT ensemble. Figure 5(a) presents that both H^S, and H^L follow an almost linear relationship with temperature, with a weak dependency of their difference on temperature. Mean enthalpies obtained from the simulations are used to estimate ΔG based on Equation (22). Figure 5(b) compares the ΔG calculated directly from MD with the linear approximation given by Equation (5), where L_0 is the enthalpy of fusion at melting point based on the predictions of interatomic potential. Aligned with our expectations based on experimental studies, $\Delta G - T$ linear relationship is held for undercooling up to 300 K, which is equivalent to 0.15×T_m. Therefore, altering the free-energy functional form in the PF model is not supported by the physics of solidification. Meanwhile, a similar process, presented in Figure 4, is repeated with solving Equation (22) using the temperature material properties. The results suggest that the limit for a linear dependency between $V - \Delta T$ is extended for up to 200K undercooling.

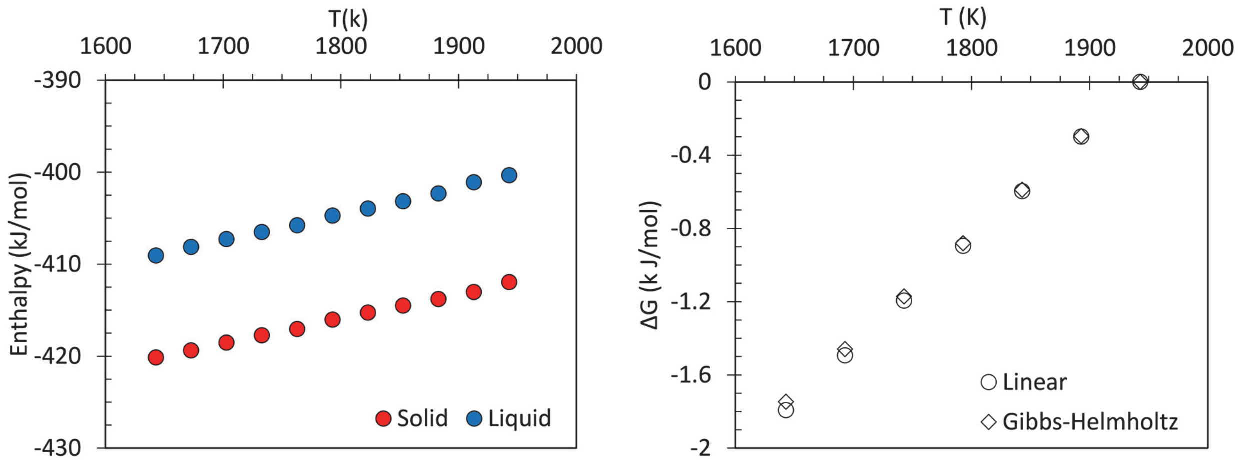

Figure 5. The variation of (a) enthalpy of solid and liquid, and (b) difference between the free energies of the solid and liquid phases with temperature.

3.3. Phase-field modeling of dendritic growth

In order to validate the PF model, we performed three-dimensional (3D) PF modeling of solidification and compared the predicted solidification-undercooling behavior, with the analytical Lipton-Kurz-Trivedi (LKT) model [52], and two sets of experiments by Walder and Ryder , and Algogo et al. We have also compared results of the current framework with the one developed by Karma and Rappel (KR model) [38]. During the solidification process, undercooling is the driving force for the phase transformation. When the solidification velocity increases, experimental data deviate from the linear behavior and present a parabolic relation with the undercooling. Results presented in Figure 6 suggest that both PF models can accurately predict the desired relationship with undercooling when ΔT<200 K. Once the undercooling increases, Karma and Rappel PF model underestimates the solidification velocity and fails to predict the experimentally observed parabolic relation between velocity and undercooling. This was expected from the 1D steady-state PF solution, as shown in Figure 4. While the current PF models predict the velocity-undercooling much closer to the experimental results.

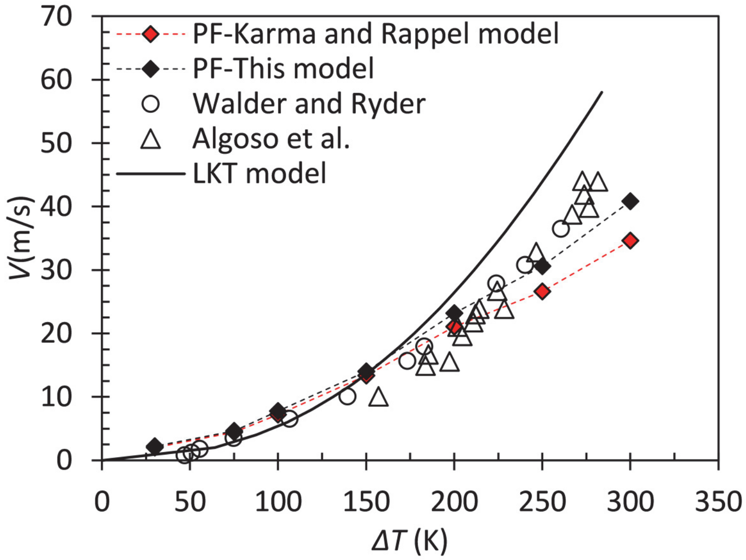

Figure 6. The variation of interface velocity versus the undercooling obtained from the PF model by Karma and Rappel [38], the current PF model, two sets of experiments by Walder and Ryder and Algoso et al. [11, 12], and analytical LKT model [52].

During the crystallization, the latent heat release increases temperature of the solid-liquid interface T_I, above the undercooling temperature [53]. Gibbs-Thomson, given by Equation **Error! Reference source not found.**, is an analytical model which relates T_I to the shape of the interface, material properties, and solidification condition [54].

$$T_I = T_M - \frac{T_M}{L}\sum_{i=1,2}\frac{1}{R_i}\left[\gamma(\hat{n}) + \frac{\partial^2\gamma(\hat{n})}{\partial\theta_i^2}\right] - \frac{V_{\hat{n}}}{\mu(\hat{n})}. \tag{25}$$

Second term on the right-hand side of Equation **Error! Reference source not found.** represents the local change of the interface equilibrium temperature due to the curvature of interface, also known as capillary undercooling. Last term on the right-hand side of Equation **Error! Reference source not found.** represents the non-equilibrium (kinetic) interface undercooling that drives the solidification. The undercooling due to curvature is only considerable for very small undercooling. Despite the smaller dendrite tip radius at large solidification velocities, capillary term is still negligible when the solidification velocities are large which leaves kinetic undercooling as the dominant undercooling term. Neglecting the effect of curvature undercooling, one obtains a linear relationship between the velocity and undercooling, where the slope gives the kinetic coefficient. This equation is used to determine the kinetic coefficient by performing MD simulation of planar growth under different solidification conditions [29, 55]. On the other hand, the experimental studies in Figure 6 suggest that for the large undercooling, *V-ΔT* relationship is parabolic, and one expects the deviation of PF results from the GT equation as the solidification velocity increases. Figure 7 shows for $\Delta T \leq 150$ K, PF results are close to the GT relation. As undercooling increases, the difference between PF and GT results increase.

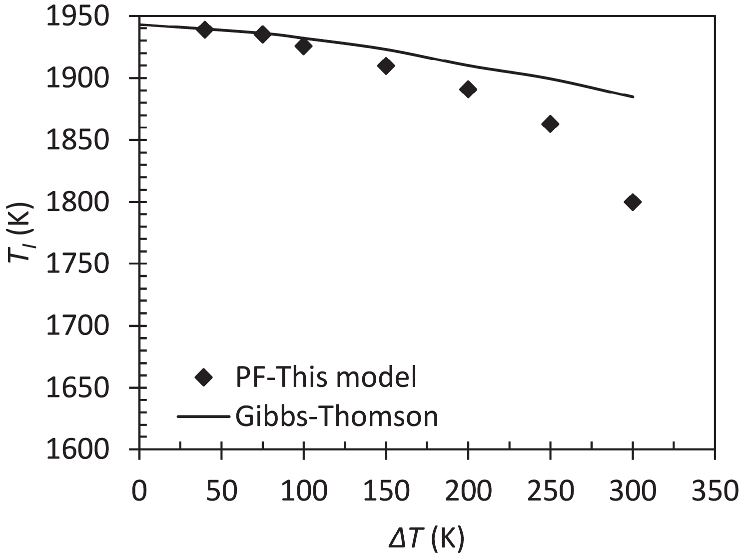

Figure 7. Comparison of the interface temperature obtained based on the current PF model with the analytical Gibbs-Thomson equation.

It has been mentioned in the literature that dendrites tend to grow along the crystallographic direction with the highest interfacial energy [56-58]. Equation (11) describes how the interface energy changes by crystallographic orientations. Based on this equation, when the δ_1 is large and δ_2 is small, disregarding δ_2 sign, dendrites grow along <100> direction. For $\delta_2 < 0$, the decrease of δ_1 increases the probability of growth direction transition from <100> to <110>. Therefore, based on the anisotropy values from MD calculations, presented in Figure 2, one may expect to observe <100>-oriented dendrites when the undercooling is small, and identify the transition of growth direction from <100> to <110> as driving force, undercooling, increases. PF simulation results based on MD-calculated anisotropies are presented in **Error! Reference source not found.**. With δ_2>0 and δ_1 >0, growth of <100> dendrites was expected for ΔT=100 K. Considering having a negative δ_2, we did not distinguish any differences between the growth rate in <100> and <110> directions for the PF simulation at ΔT=300 K. There are 2D-PF studies in the literature showing that both small anisotropy and slow solidification velocities affect the morphology types and increase the probability of seaweed structure formation [59-61].

For two target undercoolings of 100 K and 300 K, we ran different model simulations considering $\delta_1 \in (0.03, 0.05)$ and $\delta_2 \in (-0.002, 0.002)$. The results suggested that when the driving force was small and solidification velocity was slow, the anisotropy parameter plays an important role in determining the dendrite morphology. However, as the solidification velocity increases, the anisotropy parameter does not have a noticeable effect on dendrite morphology. When ΔT =300 K, the variations of δ_1 and δ_2 did not have a significant effect on orientations of dendrites as in the case with ΔT=100 K. Therefore, to have discussions on the preferred growth direction, we need to consider both the capillary and kinetic effects. Mapping of the dendrite morphology to the values of δ_2 and δ_1 , used in multiple PF simulations [6, 62, 63], is not enough for predicting the preferred growth direction, and considering both the temperature-dependent SL interface anisotropy parameters and solidification driving force (or velocity) is required.

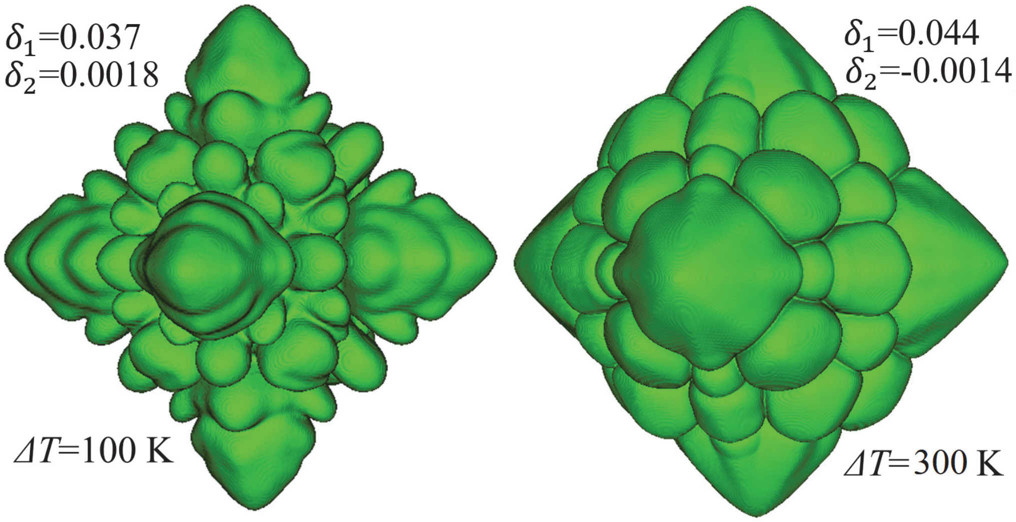

Figure 7. The dendrite morphology predicted by PF simulations based on MD-calculated anisotropies for 100 K and 300 K undercoolings.

4. Conclusion

In this study, we coupled MD and PF modeling using temperature-dependent material properties to investigate the solidification of metals. The literature PF models' limitations on predicting the rapid solidification of metals are addressed by establishing temperature-dependent anisotropic SL interfacial properties based on MD simulations and governing equations for diffusion from classical thermodynamics. We employed CFM for the points on pressure-temperature coexistence line to calculate the temperature-dependent variations of SL interface energy and anisotropy parameters. As predicted by the analytical models, the interface energy presents an almost linear relationship with temperature. Height of the double-well potential is also modified to be temperature-dependent in order to dictate the decrease of jump frequency when the working temperature decreases. After validating the proposed PF model by comparing the simulation velocity-undercooling with experimental data, we investigated the effect of MD-calculated capillary anisotropy on dendrite shape and growth direction. Based on MD simulations, it was predicted that for smaller undercooling, dendrites would be <100> oriented. As the undercooling increases, dendrite orientation shifts from <100> to <110>. While the PF results indicated that anisotropy is not the sole characteristic that should be considered in predicting growth direction; the solidification driving force is another component that should be taken into account.

Acknowledgment

This study was partially supported by the National Science Foundation, NSF-CMMI 2031800 and by NASA, 80NSSC19K0569. We are grateful for supercomputing time allocation provided by the Extreme Science and Engineering Discovery Environment (XSEDE), award number TG-DMR140008.

CRediT Author Statement

Sepideh Kavousi: Conceptualization, Methodology, Software, Formal analysis, Writing- Original draft preparation. **Austin Gates:** Methodology, Software, Formal analysis, Writing- Original draft preparation. **Lindsey Jin:** Methodology, Software, Formal analysis, Writing- Original draft preparation. **Mohsen Asle Zaeem:** Supervision, Conceptualization, Methodology, Formal analysis, Writing- Reviewing and Editing, Funding Acquisition.

Data availability

All necessary data generated or analyzed during this study are included in this published article, and other auxiliary data are available from the corresponding author on reasonable request.

Declaration of Competing Interest

The authors declare no competing interests.

References

[1] W. Kurz, D.J. Fisher, Fundamentals of solidification.
[2] M. Asta, C. Beckermann, A. Karma, W. Kurz, R. Napolitano, M. Plapp, G. Purdy, M. Rappaz, R. Trivedi, Solidification microstructures and solid-state parallels: Recent developments, future directions, Acta Materialia 57(4) (2009) 941-971.
[3] J. Dantzig, P.d. Napoli, J. Friedli, M. Rappaz, Dendritic Growth Morphologies in Al-Zn Alloys—Part II: Phase-Field Computations, Metallurgical and Materials Transactions A 44 (2013).
[4] S. Kavousi, B.R. Novak, M.I. Baskes, M. Asle Zaeem, D. Moldovan, Modified embedded-atom method potential for high-temperature crystal-melt properties of Ti–Ni alloys and its application to phase field simulation of solidification, Modelling and Simulation in Materials Science and Engineering 28(1) (2019) 015006.
[5] J.J. Hoyt, A. Karma, M.A. Asta, D.Y. Sun, From atoms to dendrites, JOM 56(4) (2004) 49-54.
[6] A. Karma, W.-J. Rappel, Quantitative phase-field modeling of dendritic growth in two and three dimensions, Physical Review E 57(4) (1998) 4323-4349.
[7] S.G. Kim, W.T. Kim, J.S. Lee, M. Ode, T. Suzuki, Large Scale Simulation of Dendritic Growth in Pure Undercooled Melt by Phase-field Model, ISIJ International 39(4) (1999) 335-340.
[8] S.-L. Wang, R. Sekerka, A. Wheeler, B. Murray, S. Coriell, R. Braun, G. McFadden, Thermodynamically-consistent phase-field models for solidification, Physica D: Nonlinear Phenomena 69(1-2) (1993) 189-200.
[9] J. Bragard, A. Karma, Y.H. Lee, M. Plapp, Linking Phase-Field and Atomistic Simulations to Model Dendritic Solidification in Highly Undercooled Melts, Interface Science 10(2) (2002) 121-136.
[10] S. Kavousi, B.R. Novak, M. Asle Zaeem, D. Moldovan, Combined molecular dynamics and phase field simulation investigations of crystal-melt interfacial properties and dendritic solidification of highly undercooled titanium, Computational Materials Science 163 (2019) 218-229.
[11] S. Walder, P.L. Ryder, A simple technique for the measurement of dendritic growth rates in undercooled metallic melts and its application to Ni and Ti, Materials Science and Engineering: A 203(1) (1995) 197-202.
[12] P. R. Algoso, A. S. Altgilbers, W. Hofmeister, R. J. Bayuzick, The Solidification Velocity of Undercooled Nickel and Titanium Alloys with Dilute Solute, 2003.
[13] R. Willnecker, D.M. Herlach, B. Feuerbacher, Evidence of nonequilibrium processes in rapid solidification of undercooled metals, Physical Review Letters 62(23) (1989) 2707-2710.
[14] J.W. Lum, D.M. Matson, M.C. Flemings, High-Speed imaging and analysis of the solidification of undercooled nickel melts, Metallurgical and Materials Transactions B 27(5) (1996) 865-870.

[15] F. Spaepen, A structural model for the solid-liquid interface in monatomic systems, Acta Metallurgica 23(6) (1975) 729-743.
[16] J.J. Hoyt, S. Raman, N. Ma, M. Asta, Unusual temperature dependence of the solid-liquid interfacial free energy in the Cu-Zr system, Computational Materials Science 154 (2018) 303-308.
[17] M. Gündüz, J.D. Hunt, The measurement of solid-liquid surface energies in the Al-Cu, Al-Si and Pb-Sn systems, Acta Metallurgica 33(9) (1985) 1651-1672.
[18] K. Keşlioğlu, N. Maraşlı, Solid–liquid interfacial energy of the eutectoid β phase in the Al–Zn eutectic system, Materials Science and Engineering: A 369(1) (2004) 294-301.
[19] K. Keşlıoğlu, M. Gündüz, H. Kaya, E. Çadırlı, Solid–liquid interfacial energy in the Al–Ti system, Materials Letters 58(24) (2004) 3067-3073.
[20] M. Erol, N. Maraşlı, K. Keşlioğlu, M. Gündüz, Solid–liquid interfacial energy of bismuth in the Bi–Cd eutectic system, Scripta Materialia 51(2) (2004) 131-136.
[21] N. Maraşlı, J.D. Hunt, Solid-Liquid surface energies in the Al_CuAl2, Al_NiAl3 and Al_Ti systems, Acta Materialia 44 (1996).
[22] Z. Jian, K. Kuribayashi, W. Jie, Solid-liquid Interface Energy of Metals at Melting Point and Undercooled State, MATERIALS TRANSACTIONS 43(4) (2002) 721-726.
[23] D. Turnbull, Formation of Crystal Nuclei in Liquid Metals, Journal of Applied Physics 21(10) (1950) 1022-1028.
[24] L. Wang, X. Lin, M. Wang, W. Huang, Anisotropic solid–liquid interfacial energy measurement by grain boundary groove method, Journal of crystal growth 406 (2014) 85-93.
[25] A. Mahata, T. Mukhopadhyay, M. Asle Zaeem, Liquid ordering induced heterogeneities in homogeneous nucleation during solidification of pure metals, Journal of Materials Science & Technology 106 (2022) 77-89.
[26] A. Mahata, M. Asle Zaeem, Size effect in molecular dynamics simulation of nucleation process during solidification of pure metals: investigating modified embedded atom method interatomic potentials, Modelling and Simulation in Materials Science and Engineering 27(8) (2019) 085015.
[27] A. Mahata, M. Asle Zaeem, M.I. Baskes, Understanding homogeneous nucleation in solidification of aluminum by molecular dynamics simulations, Modelling and Simulation in Materials Science and Engineering 26(2) (2018) 025007.
[28] J. Hoyt, M. Asta, A. Karma, Method for computing the anisotropy of the solid-liquid interfacial free energy, Physical review letters 86(24) (2001) 5530.
[29] J.J. Hoyt, M. Asta, Atomistic computation of liquid diffusivity, solid-liquid interfacial free energy, and kinetic coefficient in Au and Ag, Physical Review B 65(21) (2002) 214106.
[30] C. Qi, B. Xu, L.T. Kong, J.F. Li, Solid-liquid interfacial free energy and its anisotropy in the Cu-Ni binary system investigated by molecular dynamics simulations, Journal of Alloys and Compounds 708 (2017) 1073-1080.
[31] A.O. Tipeev, E.D. Zanotto, J.P. Rino, Diffusivity, Interfacial Free Energy, and Crystal Nucleation in a Supercooled Lennard-Jones Liquid, The Journal of Physical Chemistry C 122(50) (2018) 28884-28894.
[32] Y. Sun, F. Zhang, H. Song, M.I. Mendelev, C.-Z. Wang, K.-M. Ho, Temperature dependence of the solid-liquid interface free energy of Ni and Al from molecular dynamics simulation of nucleation, The Journal of Chemical Physics 149(17) (2018) 174501.
[33] L.-K. Wu, Q.-L. Li, M. Li, B. Xu, W. Liu, P. Zhao, B.-Z. Bai, Calculation of solid–liquid interfacial free energy and its anisotropy in undercooled system, Rare Metals 37(7) (2018) 543-553.
[34] B.B. Laird, R.L. Davidchack, Y. Yang, M. Asta, Determination of the solid-liquid interfacial free energy along a coexistence line by Gibbs–Cahn integration, The Journal of Chemical Physics 131(11) (2009) 114110.
[35] A. Karma, W.-J. Rappel, Phase-field method for computationally efficient modeling of solidification with arbitrary interface kinetics, Physical Review E 53(4) (1996) R3017-R3020.

[36] T. Suzuki, M. Ode, S.G. Kim, W.T. Kim, Phase-field model of dendritic growth, Journal of Crystal Growth 237-239 (2002) 125-131.
[37] A. Paul, T. Laurila, V. Vuorinen, S.V. Divinski, Atomic Mechanism of Diffusion, in: A. Paul, T. Laurila, V. Vuorinen, S.V. Divinski (Eds.), Thermodynamics, Diffusion and the Kirkendall Effect in Solids, Springer International Publishing, Cham, 2014, pp. 167-238.
[38] A. Karma, W.J. Rappel, Numerical Simulation of Three-Dimensional Dendritic Growth, Phys Rev Lett 77(19) (1996) 4050-4053.
[39] E. Asadi, M Asle Zaeem, S. Nouranian, M.I. Baskes, Quantitative modeling of the equilibration of two-phase solid-liquid Fe by atomistic simulations on diffusive time scales, Physical Review B 91(2) (2015) 024105.
[40] J.J. Hoyt, M. Asta, A. Karma, Method for Computing the Anisotropy of the Solid-Liquid Interfacial Free Energy, Physical Review Letters 86(24) (2001) 5530-5533.
[41] S. Plimpton, Fast Parallel Algorithms for Short-Range Molecular Dynamics, Journal of Computational Physics 117(1) (1995) 1-19.
[42] S. Kavousi, B.R. Novak, M.I. Baskes, M. Asle Zaeem, D. Moldovan, Modified embedded-atom method potential for high-temperature crystal-melt properties of Ti–Ni alloys and its application to phase field simulation of solidification, Modelling and Simulation in Materials Science and Engineering 28(1) (2019) 015006.
[43] K. Wark, Thermodynamics, McGraw-Hill, New York, 1983.
[44] E. Asadi, M. Asle Zaeem, S. Nouranian, M.I. Baskes, Quantitative modeling of the equilibration of two-phase solid-liquid Fe by atomistic simulations on diffusive time scales, Physical Review B 91(2) (2015) 024105.
[45] G.W. Lee, S. Jeon, C. Park, D.-H. Kang, Crystal–liquid interfacial free energy and thermophysical properties of pure liquid Ti using electrostatic levitation: Hypercooling limit, specific heat, total hemispherical emissivity, density, and interfacial free energy, The Journal of Chemical Thermodynamics 63 (2013) 1-6.
[46] C.V. Thompson, F. Spaepen, On the approximation of the free energy change on crystallization, Acta Metallurgica 27(12) (1979) 1855-1859.
[47] T. Frolov, Y. Mishin, Temperature dependence of the surface free energy and surface stress: An atomistic calculation for Cu(110), Physical Review B 79(4) (2009) 045430.
[48] J.W. Cahn, Interfacial segregation, Metals park (OH): American Society for Metals (1977) 11.
[49] C.A. Becker, J. Hoyt, D. Buta, M. Asta, Crystal-melt interface stresses: Atomistic simulation calculations for a Lennard-Jones binary alloy, Stillinger-Weber Si, and embedded atom method Ni, Physical Review E 75(6) (2007) 061610.
[50] N. Provatas, K. Elder, Phase-field methods in materials science and engineering, John Wiley & Sons2011.
[51] J. Kierzenka, L.F. Shampine, A BVP solver based on residual control and the Maltab PSE, ACM Transactions on Mathematical Software (TOMS) 27(3) (2001) 299-316.
[52] J. Lipton, W. Kurz, R. Trivedi, Rapid dendrite growth in undercooled alloys, Acta Metallurgica 35(4) (1987) 957-964.
[53] S. Kavousi, B.R. Novak, M. Asle Zaeem, D. Moldovan, Combined molecular dynamics and phase field simulation investigations of crystal-melt interfacial properties and dendritic solidification of highly undercooled titanium, Computational Materials Science 163 (2019) 218-229.
[54] J.J. Hoyt, M. Asta, A. Karma, Atomistic and continuum modeling of dendritic solidification, Materials Science and Engineering: R: Reports 41(6) (2003) 121-163.
[55] J. Monk, Y. Yang, M.I. Mendelev, M. Asta, J.J. Hoyt, D.Y. Sun, Determination of the crystal-melt interface kinetic coefficient from molecular dynamics simulations, Modelling and Simulation in Materials Science and Engineering 18(1) (2010) 015004.

[56] S.H. Davis, Theory of solidification, Cambridge University Press2001.
[57] J.A. Dantzig, M. Rappaz, Solidification: -Revised & Expanded, EPFL press2016.
[58] M.E. Glicksman, Principles of solidification: an introduction to modern casting and crystal growth concepts, Springer Science & Business Media2010.
[59] M. Amoorezaei, S. Gurevich, N. Provatas, Orientation selection in solidification patterning, Acta Materialia 60(2) (2012) 657-663.
[60] H. Xing, X. Dong, H. Wu, G. Hao, J. Wang, C. Chen, K. Jin, Degenerate seaweed to tilted dendrite transition and their growth dynamics in directional solidification of non-axially oriented crystals: a phase-field study, Scientific reports 6 (2016) 26625.
[61] Y. Chen, B. Billia, D.Z. Li, H. Nguyen-Thi, N.M. Xiao, A.-A. Bogno, Tip-splitting instability and transition to seaweed growth during alloy solidification in anisotropically preferred growth direction, Acta materialia 66 (2014) 219-231.
[62] J. Dantzig, P. Di Napoli, J. Friedli, M. Rappaz, Dendritic growth morphologies in Al-Zn alloys—Part II: phase-field computations, Metallurgical and Materials Transactions A 44(12) (2013) 5532-5543.
[63] L. Gao, Z. Guo, Phase-field simulation of Li dendrites with multiple parameters influence, Computational Materials Science 183 (2020) 109919.